Geophys. J. Int. (2003) **155,** 789–804

Motion of the Scotia Sea plates

Christine Thomas,[1] Roy Livermore[2] and Fred Pollitz[3]

[1] *Department of Earth Sciences, University of Liverpool,* 4 *Brownlow Street, Liverpool* L69 3GP, *UK*
[2] *British Antarctic Survey, High Cross, Madingley Road, Cambridge* CB3 0ET, *UK*
[3] *US Geological Survey,* 345 *Middlefield Road, Menlo Park,* CA 94025, *USA*

Accepted 2003 June 11. Received 2003 June 11; in original form 2002 June 14

SUMMARY

Earthquake data from the Scotia Arc to early 2002 are reviewed in the light of satellite gravity and other data in order to derive a model for the motion of plates in the Scotia Sea region. Events with magnitude $\geq$5, which occurred on or near the boundaries of the Scotia and Sandwich plates, and for which Centroid Moment Tensor (CMT) solutions are available, are examined. The newer data fill some of the previous sampling gaps along the boundaries of the Scotia and Sandwich plates, and provide tighter constraints on relative motions. Variations in the width of the Brunhes anomaly on evenly spaced marine magnetic profiles over the East Scotia Ridge provide new estimates of Scotia–Sandwich plate spreading rates. Since there are no stable fracture zones in the east Scotia Sea, the mean azimuth of sea floor fabric mapped by sidescan is used to constrain the direction of spreading. 18 new rate estimates and four azimuths from the East Scotia Ridge are combined with 68 selected earthquake slip vectors from the boundaries of the Scotia Sea in a least-squares inversion for the best-fitting set of Euler poles and angular rotation rates describing the 'present-day' motions of the Scotia and Sandwich plates relative to South America and Antarctica. Our preferred model (TLP2003) gives poles that are similar to previous estimates, except for Scotia Plate motion with respect to South America, which is significantly different from earlier estimates; predicted rates of motion also differ slightly. Our results are much more robust than earlier work. We examine the implications of the model for motion and deformation along the various plate boundaries, with particular reference to the North and South Scotia Ridges, where rates are obtained by closure.

Key words: inversion, plate motion, Scotia Sea.

1 INTRODUCTION

The Scotia Sea region is a complex collage of marginal basins surrounded by a belt of seismicity bordering the South American (SAM) and Antarctic (ANT) plates (Fig. 1). Although recognized in early plate tectonic studies as a relatively complex area (e.g. Isacks *et al.* 1968), detailed study of the region has been hampered until recently by its remoteness from earthquake recording stations and the relatively infrequent geophysical surveys capable of obtaining information concerning sea floor morphology and tectonic processes.

Forsyth (1975) performed the first comprehensive seismotectonic study of the region, and found that the first-order kinematics define a Scotia Plate (SCO), which, like the Caribbean Plate, is situated between two larger plates, from which it is separated by dominantly strike-slip boundaries; and a Sandwich Plate (SAN), which is moving rapidly eastward, forming the eastern flank of a spreading system behind the South Sandwich Arc (Fig. 1). One previous study has quantified the motions of the Scotia and Sandwich plates relative to the global plate network (Pelayo & Wiens 1989). This study used earthquake slip vectors and magnetic anomaly information to constrain a least-squares inversion using the method of Minster *et al.* (1974). Fault plane solutions determined by body wave analysis and by the CMT method (Dziewonski *et al.* 1981) were combined with SCO–SAN spreading rates estimated from marine magnetic anomalies, and 'transform' azimuths (British Antarctic Survey 1985) to perform an inversion for the relative motion of four plates (SAM, ANT, SCO, SAN). The results indicated that the data could be fitted fairly well by such a model, with SAM–ANT motion partitioned into slow W–E displacements between SAM–SCO and SCO–ANT. The model depended heavily on a fault plane solution for an earthquake southwest of South Georgia, although the SAM–SCO boundary was believed to pass to the north of the island. Removing the slip vector derived from this mechanism resulted in instability and quite a different result. Since then, a greater number of Global Digital Seismograph Network stations in the southern hemisphere has led to an increase in the number of CMT solutions available for the Scotia Sea region. Marine geophysical surveys (e.g. Livermore *et al.* 1997; Bruguier & Livermore 2001) have defined the location and form of the East Scotia Ridge and provide new constraints on SCO–SAN spreading. In this paper, we re-investigate the kinematics of the Scotia Sea region by compiling and inverting a larger and more accurate

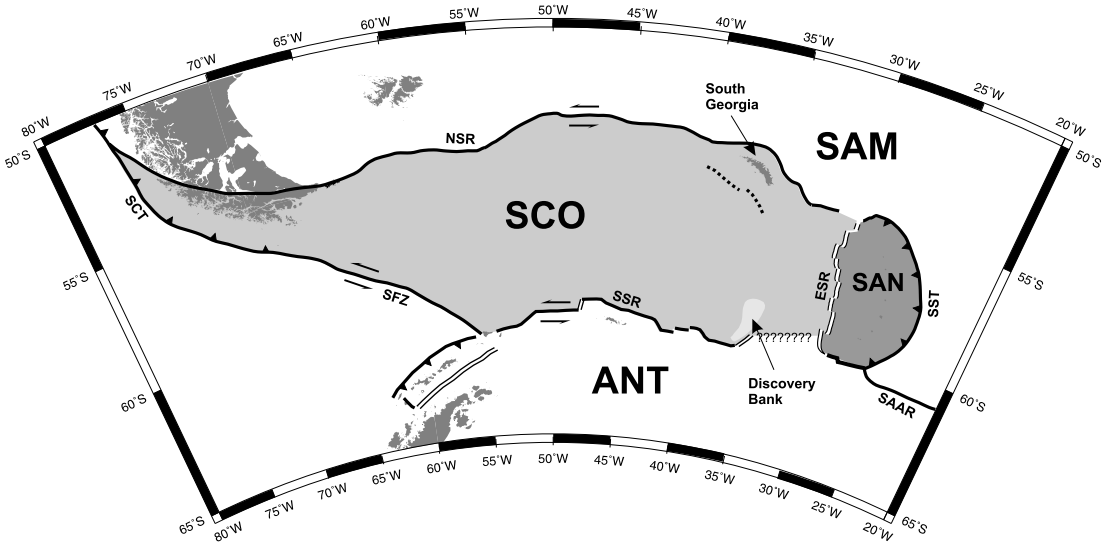

Figure 1. Plates of the Scotia Arc; locations of plate boundaries are derived from satellite gravity and earthquake data, except for East Scotia Ridge segments, which are based on swath mapping. Plate names are as follows: ANT, Antarctic Plate; SAM, South American Plate; SCO, Scotia Plate; SAN, Sandwich Plate. The location of the easternmost SCO–ANT boundary is unclear. The sense of relative plate motions is indicated by arrows. Dotted lines near South Georgia indicate the location of a shallow thrust (see the text). We have chosen a conical orthomorphic projection. SFZ: Shakleton Fracture Zone, NSR: North Scotia Ridge, ESR: East Scotia Ridge, SSR: South Scotia Ridge, SCT: Southern Chile Trench and SAAR: South American–Antarctic Ridge.

data set to obtain a new set of Euler vectors describing the four-plate system.

2 DATA

DeMets (1993) showed that the plate motion information contributed by earthquake slip vectors is entirely consistent with that supplied by transform azimuths and seafloor spreading rates, despite the difference in sampling interval. We minimize the latter by measuring average spreading rates over the Brunhes only, rather than out to Chron 2A, as was done by DeMets *et al.* (1990) in their global model. The types of constraint available for each plate boundary in the Scotia Arc region are shown schematically in Fig. 2. Rates of motion between the SCO–SAN and SAM–ANT plate pairs are available from identified magnetic anomalies on the flanks of the East Scotia Ridge (ESR) and South American—Antarctic Ridge (SAAR), respectively. No reliable direct measurements of rates of relative motion between the Scotia Sea plates (SCO, SAN) and the surrounding major plates (ANT, SAM) have yet been made, although preliminary studies using Global Positioning Satellite measurements are underway. Hence, as with Pelayo & Wiens' study, these rates are obtained by closure in our inversion.

2.1 Slip vectors

Earthquakes occurring between 1977 and early 2002 were selected from the USGS Preliminary Determination of Earthquakes catalogue within a circle of radius 30° about a point at 57°S, 45°W. Approximately 1200 events with $m_b \geq 4.5$ and focal depth between 0 and 300 km were found, from which we extracted all events with a Harvard CMT solution occurring in the Scotia Arc region between southern Chile and the Bouvet triple junction. Focal mechanisms computed by Pelayo & Wiens (1989) using body wave inversion were also examined.

Seismicity is concentrated around the margins of the Scotia Sea, with a few intraplate events, and can now be seen in the context of the

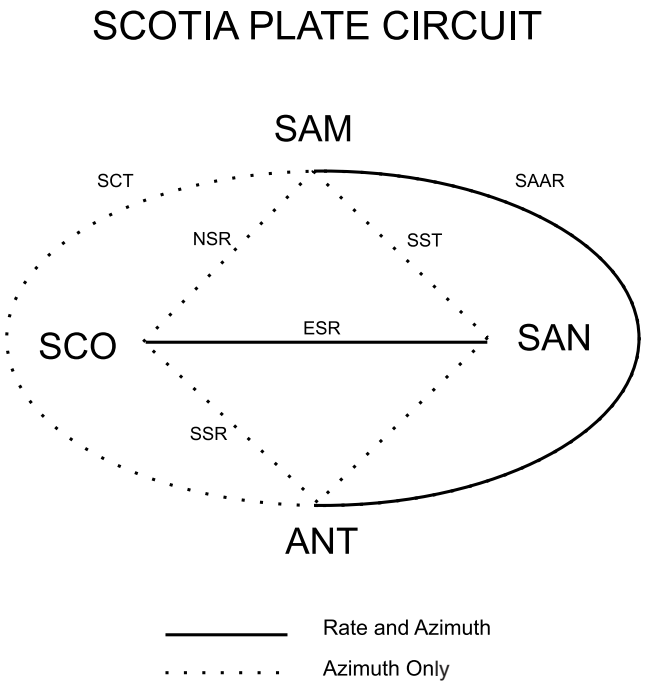

Figure 2. Network of plates in the Scotia Arc, showing the type of constraints on plate motion available from each boundary. SCT, Southern Chile Trench; SAAR, South American–Antarctic Ridge; NSR, North Scotia Ridge; SSR, South Scotia Ridge; SST, South Sandwich Trench. Solid lines show the availability of spreading rate and azimuth data, dotted lines represent boundaries for which only azimuth data (slip vectors) are available.

satellite gravity map of the Scotia Sea (Fig. 3). Earthquake numbers used in the following sections refer to those given in Table 1.

North Scotia Ridge

Event 2 (event 4 from Pelayo & Wiens (1989): PW4) from Table 1 represents sinistral slip on the eastward extension of the

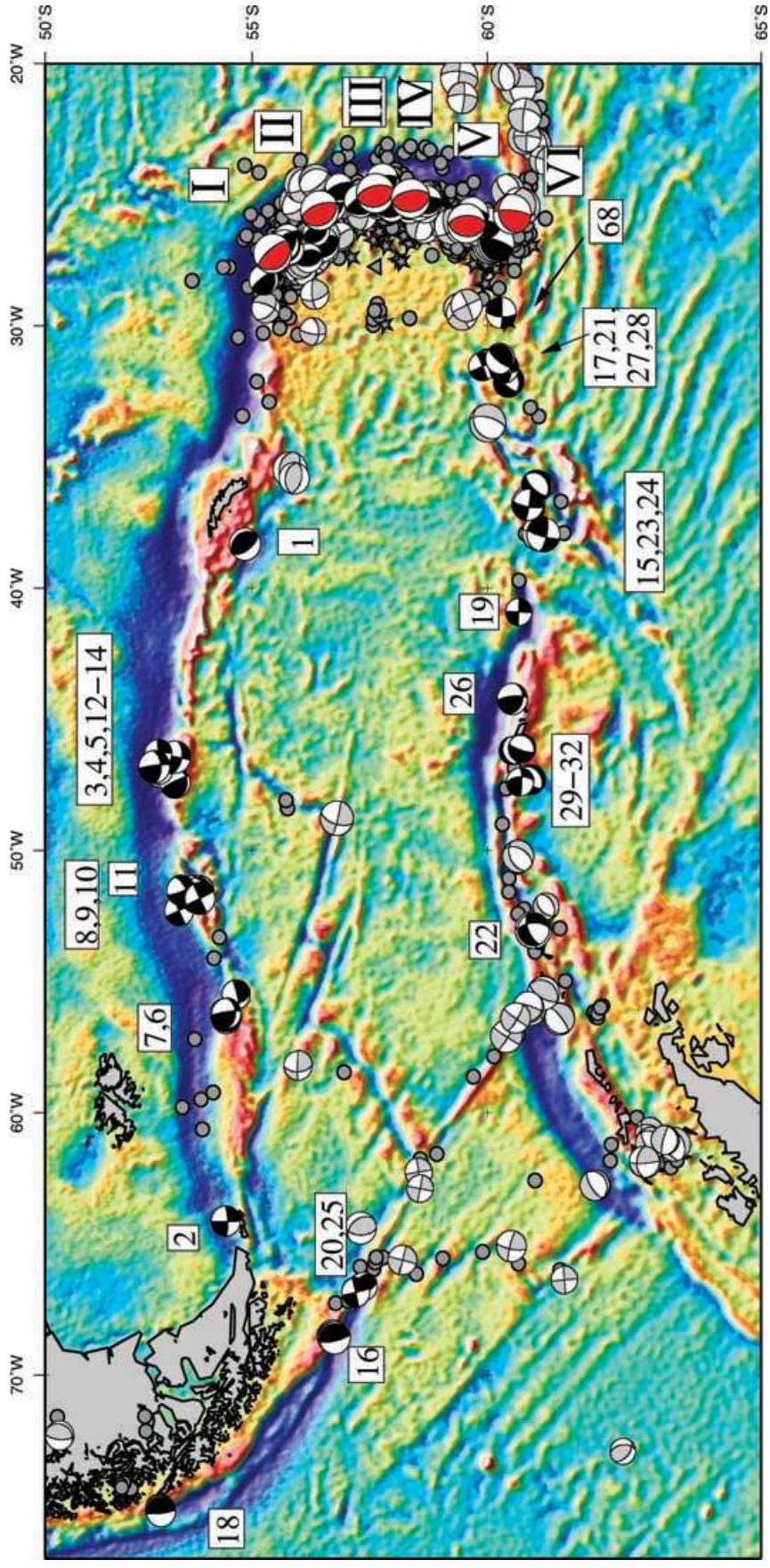

Figure 3. Lower focal spheres representing best-fitting focal mechanisms from CMTs and body wave inversion (Pelayo & Wiens 1989). Compressional sectors of focal spheres for events used in our inversion are shaded black; those not used are shaded grey. At the South Sandwich arc, focal spheres are drawn for averages of events over 1 latitude intervals (see text). Relocated epicentres of Engdahl *et al.* (1998) are shown as grey filled circles (shallow), triangles (intermediate), and stars (deep). Base map shows shaded relief of satellite-derived free-air gravity (Sandwell & Smith 1997). Numbers above focal mechanisms correspond to numbers in Table 1. Red focal mechanisms at the South Sandwich Trench show moment tensor sums (*cf.* the text and Fig. 4).

Table 1. Slip vectors (sv), spreading rates (ra) and transform azimuths (ta) and moment tensor sums (mts) used for the inversion. The slip vector gives the azimuth of motion of the first plate with respect to the second plate. The standard deviation of the data is given in σ and the predicted datum as derived from the inversion of model 2 (PRED mod2) and model 3 (PRED mod3). Earthquake parameters are from Engdahl *et al.* (1998) and for events after 1996 from the PDE (Preliminary Determination of Earthquakes) catalogue.

No	Date dd/mm/yy	Time hh:mm:ss.t	Lat.	Long.	h (km)	m_b	Plates	DAT.	PRED. mod2	PRED mod3	σ		
1	26/09/65	21:33:54.1	−54.84	−38.32	19	6.1	SAM/SCO	233	–	(246)	15	sv	PW2
2	15/06/70	11:14:50.5	−54.39	−64.13	4	5.7	SAM/SCO	269	286	285	15	sv	PW4
3	21/03/82	15:55:15.4	−53.03	−46.94	16	5.3	SAM/SCO	267	254	256	15	sv	
4	25/03/82	05:05:41.8	−52.89	−46.99	13	5.8	SAM/SCO	262	254	256	15	sv	PW12
5	30/03/82	04:24:37.3	−52.83	−46.95	17	5.1	SAM/SCO	284	254	256	15	sv	
6	18/11/82	00:27:54.9	−54.39	−56.40	25	5.7	SAM/SCO	244	272	272	15	sv	PW13
7	19/11/82	10:57:38.6	−54.40	−56.40	18	5.5	SAM/SCO	283	272	272	15	sv	
8	01/10/92	03:21:08.4	−53.62	−51.82	23	5.3	SAM/SCO	245	264	265	15	sv	
9	01/10/92	18:15:44.4	−53.64	−51.71	19	5.4	SAM/SCO	249	263	265	15	sv	
10	12/11/92	15:00:40.5	−53.79	−51.82	7	5.8	SAM/SCO	244	263	265	15	sv	
11	27/09/93	13:37:31.6	−53.72	−51.71	13	6.3	SAM/SCO	266	263	265	15	sv	
12	09/06/99	04:05:44.5	−53.04	−46.84	10	5.8	SAM/SCO	245	255	257	15	sv	
13	07/01/00	23:37:20.2	−54.33	−55.13	10	5.5	ANT/SCO	263	270	271	15	sv	
14	21/08/00	09:16:25.5	−53.02	−45.97	10	6.1	ANT/SCO	280	253	256	15	sv	
15	25/02/73	05:35:57.9	−61.09	−37.94	32	6.2	ANT/SCO	105	118	118	15	sv	PW6
16	29/12/75	03:39:43.8	−56.85	−68.58	11	6.0	ANT/SCO	77	88	87	15	sv	PW7
17	22/05/79	21:38:30.5	−60.41	−32.14	16	5.1	ANT/SCO	130	120	120	15	sv	
18	06/06/79	10:54:26.8	−52.87	−75.21	25	5.6	ANT/SCO	97	82	82	15	sv	
19	07/11/79	14:03:53.8	−60.61	−40.90	11	5.2	ANT/SCO	93	115	116	15	sv	
20	05/02/80	13:52:50.6	−57.46	−66.62	7	4.9	ANT/SCO	71	89	89	15	sv	
21	27/03/81	22:02:31.1	−59.89	−31.54	15	5.1	ANT/SCO	156	119	120	15	sv	
22	11/07/83	12:56:29.6	−60.94	−53.12	9	5.9	ANT/SCO	90	105	106	15	sv	PW16
23	09/01/84	13:43:25.5	−60.96	−36.10	10	5.4	ANT/SCO	130	119	120	15	sv	
24	13/09/86	09:28:28.2	−60.84	−36.78	25	5.8	ANT/SCO	100	118	119	15	sv	PW19
25	21/06/87	10:08:58.9	−57.29	−66.84	23	5.5	ANT/SCO	77	89	89	15	sv	
26	24/05/91	18:28:35.8	−60.49	−44.22	6	5.3	ANT/SCO	85	113	113	15	sv	
27	30/05/95	16:56:23.8	−60.32	−31.59	15	5.5	ANT/SCO	99	120	120	15	sv	
28	15/06/95	18:58:11.0	−60.25	−31.24	10	4.8	ANT/SCO	128	120	120	15	sv	
29	15/11/98	13:27:04.1	−60.28	−47.48	10	5.5	ANT/SCO	125	111	111	15	sv	
30	17/07/99	22:26:08.4	−60.20	−47.47	33	5.4	ANT/SCO	86	110	111	15	sv	
31	14/10/00	20:38:56.7	−60.19	−46.81	10	5.3	ANT/SCO	159	111	112	15	sv	
32	26/11/00	23:09:58.6	−60.23	−47.07	10	5.2	ANT/SCO	107	112	112	15	sv	
33	14/09/77	14:51:05.7	−56.43	−25.69	40	5.7	SAM/SAN	249	259	–	15	sv	
34	07/03/78	23:31:29.6	−56.58	−25.67	21	5.7	SAM/SAN	269	259	–	15	sv	
35	10/03/78	03:49:30.9	−56.69	−25.47	51	5.3	SAM/SAN	259	258	–	15	sv	
36	27/11/78	09:43:22.3	−57.99	−25.30	15	5.7	SAM/SAN	269	259	–	15	sv	
37	27/10/79	04:04:45.1	−58.82	−25.25	13	5.4	SAM/SAN	241	259	–	15	sv	
38	12/11/82	00:08:56.4	−55.86	−26.87	20	5.4	SAM/SAN	248	261	–	15	sv	
39	25/05/84	21:49:51.0	−60.21	−26.86	13	5.7	SAM/SAN	247	262	–	15	sv	
40	26/12/84	09:38:02.2	−58.74	−25.51	41	5.6	SAM/SAN	271	259	–	15	sv	
41	22/02/85	09:33:37.8	−55.80	−26.69	17	5.7	SAM/SAN	289	260	–	15	sv	
42	16/03/85	08:19:09.5	−55.26	−28.24	12	5.3	SAM/SAN	232	263	–	15	sv	
43	15/05/85	20:12:45.6	−56.72	−25.40	19	5.7	SAM/SAN	264	258	–	15	sv	
44	01/08/85	23:15:15.5	−57.77	−25.36	22	5.4	SAM/SAN	261	259	–	15	sv	
45	05/09/85	08:37:44.0	−56.93	−24.74	12	5.1	SAM/SAN	248	257	–	15	sv	
46	14/04/86	14:52:13.1	−57.86	−24.45	14	5.5	SAM/SAN	262	257	–	15	sv	
47	20/06/86	18:41:30.3	−58.70	−25.11	32	5.8	SAM/SAN	288	259	–	15	sv	
48	02/07/86	12:53:05.5	−59.62	−26.08	19	5.3	SAM/SAN	270	260	–	15	sv	
49	14/11/86	06:33:24.9	−58.77	−25.24	19	5.5	SAM/SAN	266	259	–	15	sv	
50	18/11/86	12:02:28.6	−57.96	−25.34	58	5.4	SAM/SAN	262	259	–	15	sv	
44	27/12/86	02:43:56.4	−56.26	−27.41	36	5.6	SAM/SAN	256	262	–	15	sv	
45	30/01/87	22:29:38.9	−60.17	−26.85	9	6.1	SAM/SAN	288	262	–	15	sv	
46	18/02/87	10:32:16.1	−55.84	−27.09	31	5.6	SAM/SAN	247	261	–	15	sv	
47	23/02/87	02:43:42.1	−58.01	−25.34	32	6.0	SAM/SAN	264	259	–	15	sv	
48	28/03/87	05:04:13.3	−58.06	−25.50	36	5.4	SAM/SAN	270	259	–	15	sv	
49	14/04/87	17:20:42.7	−58.41	−25.51	40	5.6	SAM/SAN	261	259	–	15	sv	
50	09/07/87	07:27:33.6	−56.46	−25.68	18	5.6	SAM/SAN	263	259	–	15	sv	
51	27/12/86	02:43:56.4	−56.26	−27.41	36	5.6	SAM/SAN	256	262	–	15	sv	
52	30/01/87	22:29:38.9	−60.17	−26.85	9	6.1	SAM/SAN	288	262	–	15	sv	
53	18/02/87	10:32:16.1	−55.84	−27.09	31	5.6	SAM/SAN	247	261	–	15	sv	

Table 1. (*Continued.*)

No	Date dd/mm/yy	Time hh:mm:ss.t	Lat.	Long.	h (km)	m_b	Plates	DAT.	PRED. mod2	PRED mod3	σ		
54	23/02/87	02:43:42.1	−58.01	−25.34	32	6.0	SAM/SAN	264	259	–	15	sv	
55	28/03/87	05:04:13.3	−58.06	−25.50	36	5.4	SAM/SAN	270	259	–	15	sv	
56	14/04/87	17:20:42.7	−58.41	−25.51	40	5.6	SAM/SAN	261	259	–	15	sv	
57	09/07/87	07:27:33.6	−56.46	−25.68	18	5.6	SAM/SAN	263	259	–	15	sv	
58	29/08/87	14:15:19.7	−56.56	−25.65	28	6.0	SAM/SAN	259	259	–	15	sv	
59	17/04/88	05:11:34.1	−58.59	−25.37	15	5.5	SAM/SAN	261	259	–	15	sv	
60	10/07/88	19:51:06.5	−56.43	−26.42	34	5.2	SAM/SAN	248	260	–	15	sv	
61	02/08/88	22:08:33.8	−58.09	−25.23	29	5.3	SAM/SAN	254	259	–	15	sv	
62	01/11/88	22:31:08.1	−57.39	−25.22	14	6.0	SAM/SAN	254	258	–	15	sv	
63	09/12/88	07:49:28.7	−59.96	−26.05	43	5.5	SAM/SAN	280	260	–	15	sv	
64	08/02/89	23:46:44.0	−55.72	−26.91	29	5.5	SAM/SAN	227	261	–	15	sv	
65	18/08/89	03:46:24.1	−55.36	−28.04	9	5.6	SAM/SAN	271	263	–	15	sv	
66	21/11/92	22:39:33.1	−56.55	−26.89	14	6.0	SAM/SAN	257	261	–	15	sv	
67	09/03/93	07:45:43.9	−59.70	−25.71	22	5.8	SAM/SAN	276	260	–	15	sv	
68	20/05/79	03:02:30.7	−60.27	−29.49	11	5.6	ANT/SAN	273	264	259	15	sv	
69	–	–	− 57.39	−30.20	–	–	SCO/SAN	6.693	6.558	6.548	0.4	ra	
70	–	–	− 57.29	−30.21	–	–	SCO/SAN	6.532	6.538	6.524	0.4	ra	
71	–	–	−57.18	−30.22	–	–	SCO/SAN	6.662	6.516	6.498	0.4	ra	
72	–	–	−56.85	−30.73	–	–	SCO/SAN	6.436	6.450	6.414	0.4	ra	
73	–	–	−56.75	−30.76	–	–	SCO/SAN	6.307	6.429	6.390	0.4	ra	
74	–	–	−56.64	−30.75	–	–	SCO/SAN	6.178	6.407	6.363	0.4	ra	
75	–	–	−56.53	−30.75	–	–	SCO/SAN	6.372	6.385	6.337	0.4	ra	
76	–	–	−56.42	−30.74	–	–	SCO/SAN	6.404	6.362	6.310	0.4	ra	
77	–	–	−56.10	−30.41	–	–	SCO/SAN	6.013	6.296	6.236	0.4	ra	
78	–	–	−55.99	−30.41	–	–	SCO/SAN	6.275	6.273	6.209	0.4	ra	
79	–	–	−57.91	−29.85	–	–	SCO/SAN	6.561	6.663	6.676	0.4	ra	
80	–	–	−58.04	−29.83	–	–	SCO/SAN	6.854	6.690	6.707	0.4	ra	
81	–	–	−58.17	−29.84	–	–	SCO/SAN	6.725	6.716	6.738	0.4	ra	
82	–	–	−58.31	−29.81	–	–	SCO/SAN	6.850	6.744	6.772	0.4	ra	
83	–	–	−58.44	−29.86	–	–	SCO/SAN	7.047	6.770	6.802	0.4	ra	
84	–	–	−58.86	−29.86	–	–	SCO/SAN	6.928	6.854	6.902	0.4	ra	
85	–	–	−59.25	−29.62	–	–	SCO/SAN	6.852	6.932	6.996	0.4	ra	
86	–	–	−59.52	−29.59	–	–	SCO/SAN	6.758	6.985	7.060	0.4	ra	
87	–	–	−56.50	−30.50	–	–	SAN/SCO	89.9	91	86	10	ta	
88	–	–	−57.50	−30.00	–	–	SAN/SCO	81.3	90	85	10	ta	
89	–	–	−58.50	−30.00	–	–	SAN/SCO	87.8	90	85	10	ta	
90	–	–	−59.50	−29.60	–	–	SAN/SCO	84.0	89	85	10	ta	
91	–	–	−55.50	−27.00	–	–	SAM/SAN	230	–	256	15	mts	I
92	–	–	−56.50	−25.00	–	–	SAM/SAN	251	–	253	15	mts	II
93	–	–	−57.50	−25.00	–	–	SAM/SAN	258	–	253	15	mts	III
94	–	–	−58.50	−25.30	–	–	SAM/SAN	259	–	254	15	mts	IV
95	–	–	−59.50	−26.00	–	–	SAM/SAN	267	–	–	15	mts	V
96	–	–	−60.50	−26.00	–	–	SAM/SAN	276	–	–	15	mts	VI

Magallanes Fault Zone (Pelayo & Wiens 1989; Klepeis 1994). Beneath Burdwood Bank, event 6 (PW13) has been interpreted as implying sinistral strike-slip on a shallow-dipping extension of a decollement observed on seismic profiles (Ludwig & Rabinowitz 1982). Event 7 is a small event rejected by Pelayo & Wiens because of its low signal-to-noise ratio.

Between 1992 October and 1993 September, four shallow (<20 km) events occurred near 53.6°S, 51.7°W (events 8–11). Three correspond to sinistral, strike-slip motion on subvertical faults striking ENE, and one to W–E, sinistral, strike-slip motion on a fault plane dipping gently to the south. All are located near the northern margin of the free-air high representing the structural block of the North Scotia Ridge: recent relocation (Engdahl *et al.* 1998) moves them west by 10–20 km (Fig. 3). Assuming W–E motion of SAM–SCO, as predicted by Pelayo & Wiens (1989), this section of the NSR would be expected to exhibit a transtensional character. However, it appears that the seismic activity records mainly strike-slip movements on faults subparallel to the margin. Recent long-range sidescan sonar imaging with GLORIA has shown the presence of a series of steep, probably active, ENE-trending faults at the contact between the North Scotia Ridge and the accreted sediments to the north (Cunningham *et al.* 1998), close to these epicentres. Hence, the contact appears to be the locus of present-day SAM–SCO motion along this part of the North Scotia Ridge.

It is curious that no events have been recorded between 46°W and 34°W, including South Georgia. This may be attributable to the low frequency of earthquakes associated with slow plate motions, although existing models of SAM–SCO motion imply that South Georgia is located at a restraining bend in the North Scotia Ridge, and might therefore be expected to experience a significant amount of thrusting. On the other hand, a large event has been recorded to the southwest of the South Georgia block (event 1; PW2). This event

proved crucial in obtaining the plate motion solution of Pelayo & Wiens (1989), and indicates SW-directed thrusting of South Georgia over the Scotia Plate. This interpretation is supported by very recent activity at the southeastern margin of the South Georgia block. Satellite-derived free-air gravity provides clues to the origin of this thrusting (Fig. 3). A pronounced linear free-air low trends NW–SE, approximately perpendicular to the slip vector of event 1, and appears to be offset to the east near 37.5°W, continuing SE with lower amplitude to 56.5°S, 35°W, where it intersects a narrow, NE-trending linear free-air high. Other NE-trending lineaments appear to transect the South Georgia block between this high and South Georgia island.

Shackleton Fracture Zone

Most events on or near the Shackleton Fracture Zone occur in three zones: close to the southeastern termination in the vicinity of Elephant Island; between 61° and 63°W, near the junction with the inactive West Scotia Ridge spreading centre; and between 65° and 68°W, at the junction with the former Phoenix (PHX)–Antarctic spreading centre.

In their plate motion inversion, Pelayo & Wiens (1989) rejected all events from near the Elephant Island triple junction, on account of suspected microplate motions in this region. Klepeis & Lawver (1996) suggest that a new SCO–ANT boundary may be forming within the Scotia Sea to the north of Elephant Island, based upon their identification of a lineament in the satellite free-air gravity field. However, there is very little earthquake evidence for this.

Several of the events between 66°W and Elephant Island are strike-slip events with one nodal plane subparallel to the Shackleton Fracture Zone. This suggests either that deformation is strongly influenced by the trend of the pre-existing fracture zone (FZ), or that the Phoenix Plate is still experiencing independent motion involving slow spreading at the PHX–ANT ridge. Recent work dates Phoenix Ridge extinction at chron C2A (3.3 Ma; Livermore *et al.* 2000), so that the former explanation seems more likely.

South Scotia Ridge

Events on the SSR appear rather less clustered than on the NSR. Epicentres occur in a narrow band associated with the pronounced free-air gravity lows within the westernmost South Scotia Ridge and to the north of South Orkney (Fig. 3). Several of these exhibit characteristic normal faulting mechanisms, reflecting the transtensional nature of the plate boundary. The absence of seismic activity within Powell Basin supports the notion that significant relative motion between the South Orkney Microcontinent and the Antarctic Peninsula has ceased, the major phase of spreading coming to an end in the Early Miocene (King *et al.* 1997; Eagles & Livermore 2002).

Pelayo & Wiens (1989) used focal mechanisms west of 50°W and at Discovery Bank in their inversion. Between these areas, two additional mechanisms are shown in Fig. 3, corresponding to events not used by Pelayo & Wiens. Event 26 is a small ($m_b = 5.3$), shallow event that occurred in 1991 to the northeast of the South Orkney Islands. The CMT solution indicates thrusting on a fault plane dipping gently beneath the South Orkney block, with a significant component of sinistral strike-slip. The trend of this part of the SCO–ANT margin would lead to its forming a restraining bend (assuming W–E plate motion), which may explain the deep free-air low associated with it. Event 19 indicates sinistral strike-slip motion along the axis of the W–E-trending trough, which bounds the NE corner of South Orkney. Near Discovery bank, mechanisms indicate predominantly NW–SE motion, which varies from low-angle thrusting (event 28) to normal faulting (event 17).

South Sandwich Trench

The majority of earthquake events in the Scotia Arc occur at the South Sandwich Trench, in particular near its northern end (Fig. 3). Between 56° and 59°S, events shallower than 60 km are predominantly of thrust type, with more strike-slip and complex mechanisms near the ends of the trench, where a distinct trench-normal bias is apparent in the earthquake slip vectors.

A global analysis by Frohlich & Apperson (1992) showed that such shallow interplate events at subduction zones have a high degree of internal consistency, relatively simple fault geometry and reflect the plate convergence direction strongly. We performed an analysis of earthquakes at the South Sandwich Trench up to 1997 based on Frohlich & Apperson's methods. Events shallower than 60 km were divided into 1° latitude bins. For each bin, the moment sum, seismic consistency C_s and the compensated linear vector dipole parameter f_{clvd} were calculated (Fig. 4; Table 2). The ratio f_{clvd} varies from zero for a pure double-couple source to 0.5 for a pure compensated linear vector dipole (CLVD, Frohlich & Apperson 1992).

This ratio is less than 0.10 for all except one tensor sum and all values are reduced compared with the ratios for individual events (Fig. 4, bottom). The results show high consistency between latitudes 56° and 59°S, slightly less at the northern end, and rather poor consistency south of 59°S (Table 2). Perhaps surprisingly, slip vectors corresponding to these moment sums (Fig. 3, I–VI) still show some trench-normal bias. This suggests that a component of SAM–SAN convergence may be taken up aseismically or by events that are too small to be recorded teleseismically. Much of this deformation could be occurring in the forearc, as a result of the increasingly oblique plate convergence towards the extremities of the trench, as suggested for subduction zones elsewhere (Jarrard 1986; Ekström & Engdahl 1989; McCaffrey 1992). These averages were used to constrain the SAM–SAN vector in the plate motion inversion (see below).

Two large normal faulting events in the forearc region were eliminated from the 'restricted' data sets, owing to the likelihood of their being related to disruption of the outer forearc rather than directly reflecting SAM–SAN motion. This disruption could be related to the subduction of NW-trending fracture zone ridges and troughs observed in the free-air gravity anomaly field (Fig. 3), which, being subparallel to the trench, might cause periodic uplift of the forearc.

East Scotia Ridge

Seismicity on the East Scotia Ridge is generally low, with a small cluster of events near the deepest part of the ridge, at the offset between segments E5 and E6 (Fig. 5), on the eastern flank of the ridge. Two shallow epicentres occur on the axis of segment E2, a southwards-propagating rift (Livermore *et al.* 1997), one of which lies close to the inflated middle section of the segment (Fig. 3), while the other is located near the rift tip. It is likely that these events are associated with simple shear deformation associated with migrating non-transform offsets (Wetzel *et al.* 1993), and so do not constrain the azimuth of plate motion. Events for which CMT solutions are available include three large ($m_b = 5.3$–5.7) events, which occurred in 1983, 1986 and 1989 on segment E8, close to a pronounced axial topographic high (Bruguier & Livermore 2001). Whether these

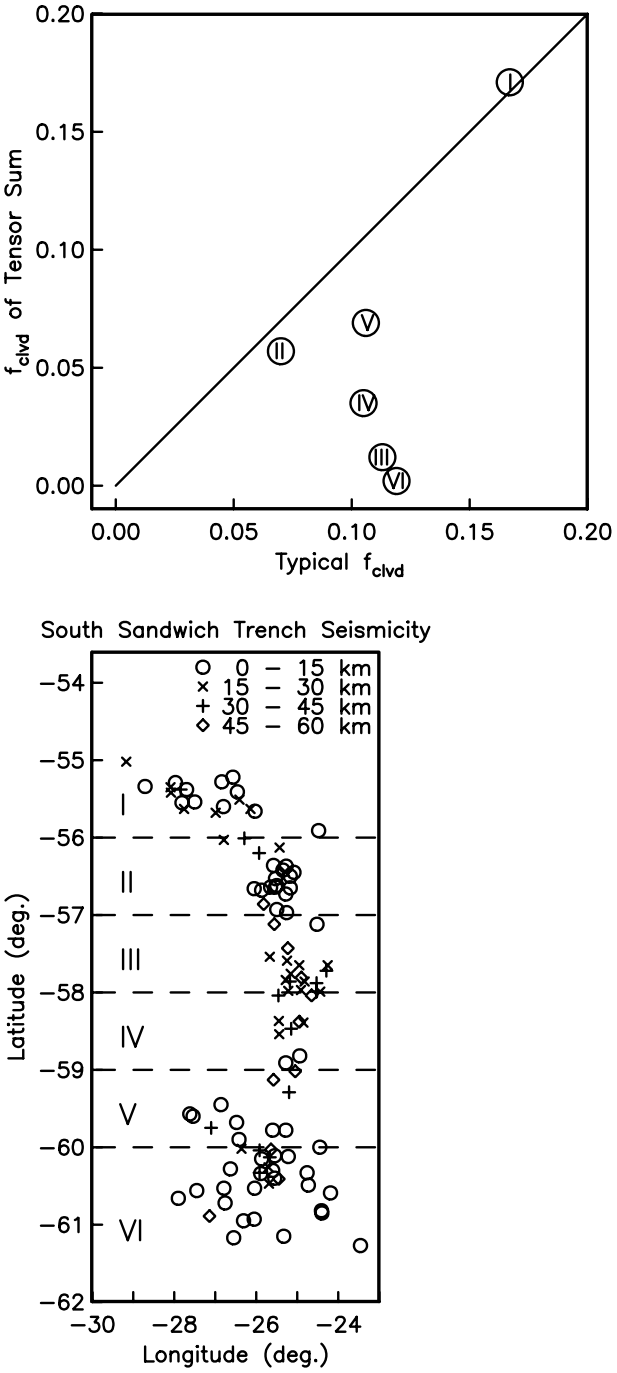

Figure 4. Analysis of South Sandwich events using the methods of Frohlich & Apperson (1992). (a) Typical f_{clvd} (average for a particular subregion) versus f_{clvd} for the summed moment tensor of that subregion. All earthquakes considered have been normalized to unit moment prior to averaging. In all cases but one (Region I) this ratio is reduced in the sum; hence the tensor sums are more double-couple-like. (b) Epicentres of all earthquakes in the Harvard CMT catalogue through 1997 associated with the South Sandwich trench up to a depth of 60 km. In order to avoid possible intra-South Sandwich plate deformation, it is required that all eligible epicentres lie at least 250 km away from the centre of curvature of the arc at 57.5°S, 30.0°W. Earthquakes are binned according to indicated latitude windows ranging from I to VI (northern part to southern part).

Table 2. Compensated linear vector dipole parameter f_{clvd} for the South Sandwich events. Φ_s, δ and λ: strike of nodal plane, dip and rake as defined by Aki & Richards (1980) (pp. 114–115). ϵ: strike of horizontal component of slip vector in degrees clockwise from North C_s: seismic consistency parameter (Frohlich & Apperson 1992).

Region	Plane 1				Plane 2				No events	C_s
	Φ_s	δ	λ	ϵ	Φ_s	δ	λ	ϵ		
I	148	20	98	50	320	71	87	−122	19	0.65
II	147	26	78	71	341	65	96	−122	21	0.79
III	164	30	87	78	348	60	92	−106	18	0.79
IV	172	32	92	79	349	58	88	−98	9	0.89
V	187	35	98	87	357	56	85	−83	12	0.32
VI	250	30	150	96	6	75	63	−20	32	0.39

earthquakes were caused by magma migration or deformation is not known, but they do not appear to constrain plate motions. A strike-slip event on E4, close to an oblique lineament, probably reflects simple shear deformation associated with a migrating non-transform offset. Hence, earthquake seismology provides no useful constraints on the direction of spreading at the SCO–SAN boundary.

One of the focal planes of event 68 implies a right-lateral strike-slip earthquake, which could represent SAN–ANT relative motion. Sidescan sonar imagery (Bruguier & Livermore 2001) indicates that a transform boundary connects with the southern tip of the East Scotia Ridge, from where it runs eastward, possibly to connect with rifts within the South Sandwich Arc, and ultimately with the South Sandwich Fracture Zone to the southeast. The original Harvard CMT hypocentre places this event some 30 km north of this transform, but non-linear relocation (Engdahl *et al.* 1998) places it within 15 km of the transform, close to the ridge–transform intersection. Moreover, the strike of the W–E nodal plane is parallel to the trend of the transform, and the right-lateral sense is in agreement with that expected for SAN–ANT motion. The use of a radially symmetrical Earth model can give rise to errors of up to 50 km in the vicinity of lateral heterogeneities such as subducted slabs (Engdahl & Gubbins 1987), so that it seems likely that this event actually reflects motion on the transform. We have therefore used the slip vector associated with this event to constrain SAN–ANT motion.

Intraplate events

Significant within-plate events have been identified previously (Forsyth 1975; Pelayo & Wiens 1989), including a strike-slip earthquake (PW20) on the Endurance Fracture Zone, close to the inside corner of its eastern ridge–transform intersection, and a more recent event on the western Quest Fracture Zone. Other shallow events, without CMTs, lie near the axis of the West Scotia Ridge to the north and west. Analysis of magnetic anomalies over the Ridge indicate extinction at approximately 6.5 Ma (Barker & Burrell 1977; Livermore *et al.* 1994), so that these events may be related to post-spreading stress release. We therefore exclude them from our study, and assume a single, rigid, Scotia Plate.

West of the Shackleton FZ, the former Phoenix–Antarctic plate boundary is delineated by a series of shallow events connecting the Shackleton and Hero FZs. We can now see that seismicity is concentrated on the axis of the Phoenix Ridge (Fig. 3), an intermediate rate spreading centre that is thought to have slowed and ceased opening by about 3.3 Ma (Larter & Barker 1991; Livermore *et al.* 2000). The relatively high seismicity suggests a significant amount of relict activity on this boundary, with strike-slip mechanisms rotated relative

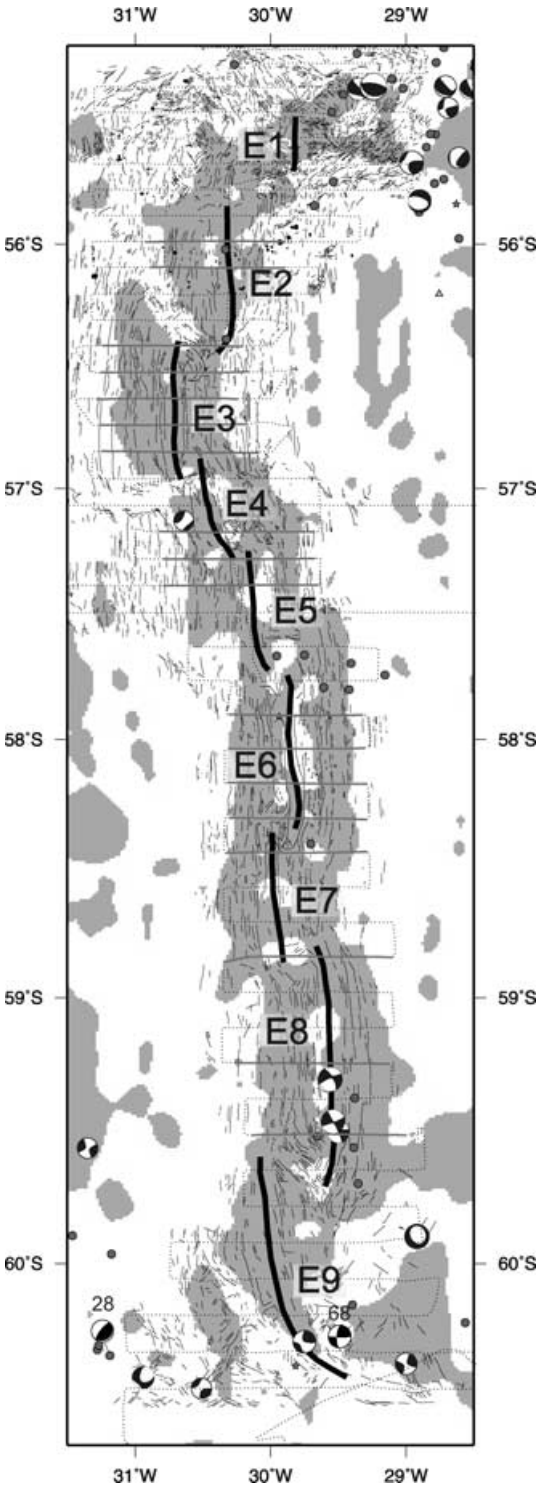

Figure 5. Seafloor lineaments on the flanks of the East Scotia Ridge picked from sidescan sonar images; areas of positive magnetic polarity are shaded; the ridge axis is denoted by thick lines. Earthquake CMT solutions are shown as in Fig. 3; grey dots are relocated epicentres of Engdahl *et al.* (1998). Track of vessel RRS James Clark Ross during cruise JR09 is shown by dotted line; magnetic anomaly crossings of axis used in computing spreading rates are highlighted in grey.

to the fracture zone trend, perhaps induced by stresses related to continuing subduction at the South Shetland Trench.

2.2 Spreading rates

At present, the only rate information comes from the East Scotia Ridge, an intermediate-rate spreading centre with well-developed magnetic anomalies, which forms the SCO–SAN boundary. This information is crucial to our inversion as it determines the rates on all of the other boundaries of the SCO or SAN plates by closure.

Using evenly spaced magnetic profiles obtained during a recent survey of the East Scotia Ridge, we picked the steep gradients marking the limits of normally magnetized crust formed during the Brunhes epoch, the start of which is dated at 778 kyr (Tauxe *et al.* 1996). At these latitudes, the magnetization vector is steep and the error in using the magnetic anomaly to estimate the width of the source body is small. Assuming W–E spreading, we measured the distance between the picks on all profiles where the Brunhes anomaly was clear. Evidence from sidescan mapping (see below) indicates that this is probably within 5° of the true spreading direction, amounting to a maximum rate error of 0.01 mm yr^{-1}. This resulted in 18 estimates of mean spreading rate for the Brunhes, each of which was assigned to the ridge axis location as observed on the corresponding profile (Table 1, 69–86). Despite ridge offsets and changes in the Brunhes magnetic signature, these measurements appear to define a trend of increasing rates from about 60 mm yr^{-1} at the northern end of the East Scotia Ridge, to a maximum of about 70 mm yr^{-1} near 58°30′S, declining slowly thereafter (Fig. 6), consistent with a distant SCO–SAN Euler pole.

2.3 Spreading azimuths

The data set of Pelayo & Wiens (1989) included 'transform' azimuths measured from a map of east Scotia Sea bathymetry and magnetic isochrons (British Antarctic Survey 1985). More recent satellite gravity maps (e.g. Fig. 3) show a series of WNW-trending lineaments on the western flank of the East Scotia Ridge. Their eastern flank counterparts are obscured by a thick volcaniclastic apron (Barker & Hill 1981), but an ENE trend is discernible. This pattern has been interpreted as evidence for a southward migration of ridge offsets throughout the evolution of the East Scotia Ridge (Livermore *et al.* 1994), and precludes the use of these gravity lineaments to establish flow lines of SCO–SAN motion. Recent

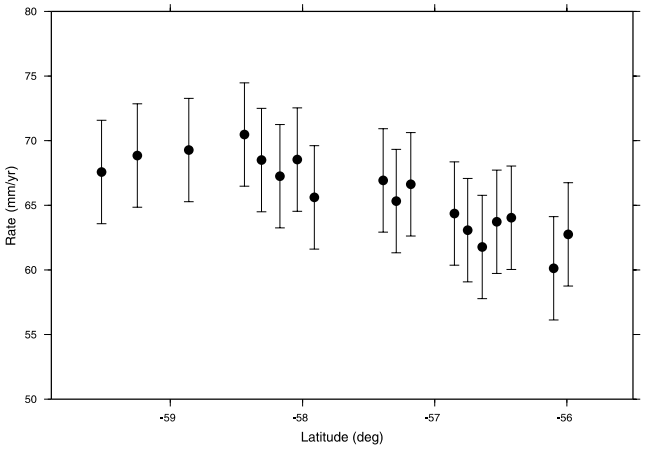

Figure 6. Spreading rates along the East Scotia Ridge derived from the width of the Brunhes. Error bars represent an assumed uncertainty of ±4 mm yr^{-1}.

detailed mapping of the East Scotia Ridge (Fig. 5) shows that it does not have true transform offsets, but is characterized by overlapping and/or propagating spreading centres.

We have made the assumption that spreading was perpendicular to the well-defined seafloor fabric mapped by sidescan sonar (Fig. 5). This assumption would be invalid if significant oblique spreading were occurring here (Taylor *et al.* 1994). However, we note that, at intermediate and fast rates, spreading is generally perpendicular to the strike of the ridge axis, and even where oblique spreading occurs, such as on the slow-spreading Reykjanes Ridge, the fabric observed on the ridge flanks tends to be less oblique than the ridge itself (Applegate & Shor 1994).

Lineaments interpreted as sea floor faults and volcanic ridges were picked from sidescan images and digitized, and their azimuths and lengths determined. These were binned with a continuous weighting function, and directional statistics calculated (Fig. 7). Although there is subjective bias in this procedure, the W–E survey tracks tend to suppress ridge-parallel features in the sonar images, thereby reducing the chances of picking such features at the expense of features with other orientations. These averages were calculated for 1° latitude bands within the Brunhes, as defined by positive magnetic anomalies along the ridge, for inclusion in our inversion (Table 1, 87–90). In the northernmost and southernmost intervals, complex deformation results in a broad spread of azimuths, so that

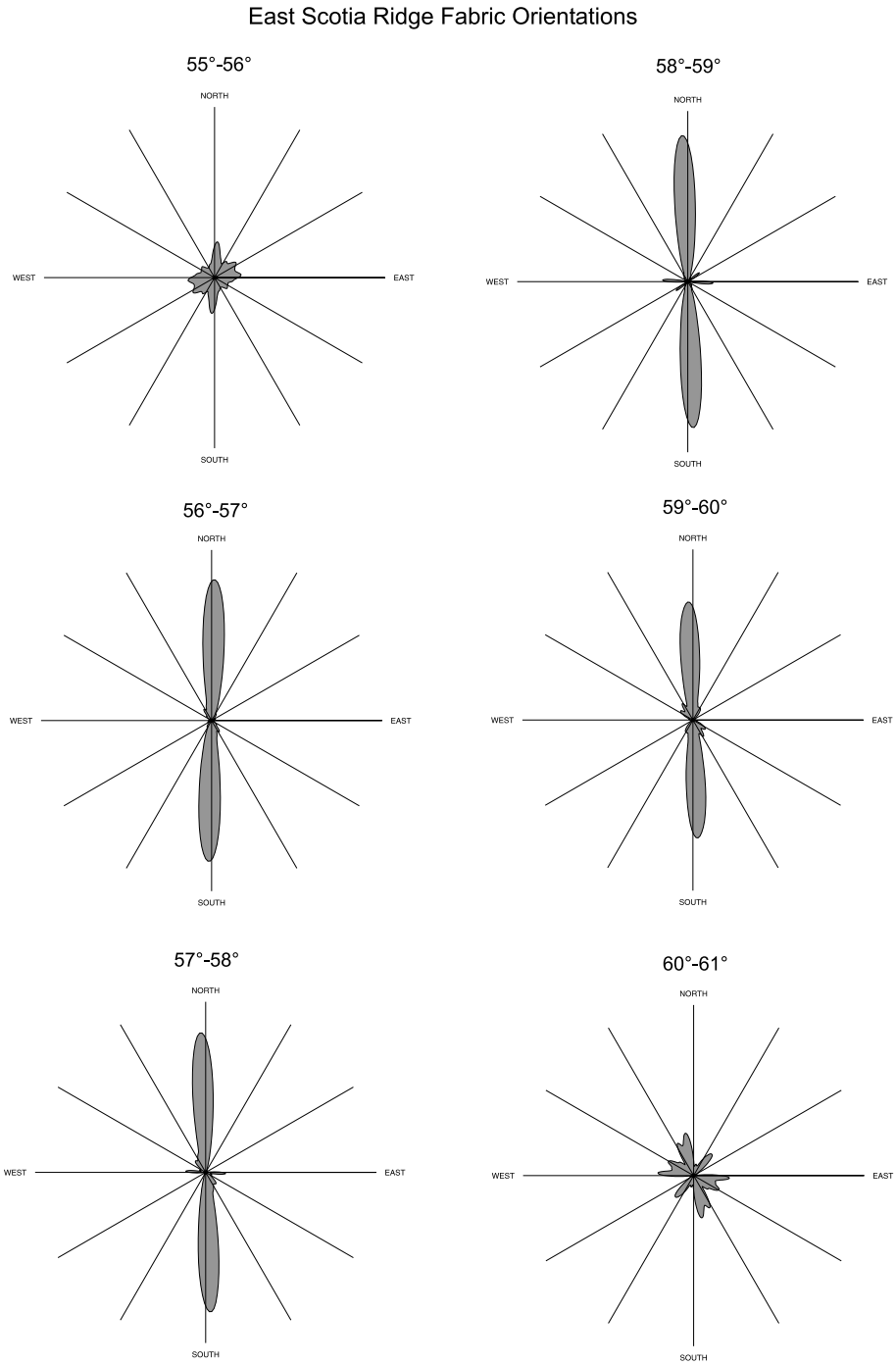

Figure 7. Azimuthal distribution of lineaments picked from sidescan sonar in 1° latitude intervals. See the text for details.

statistically significant means could not be determined, but the others all show strong modes close to N–S. In these cases, the standard errors are used as the data uncertainties in our inversion.

3 INVERSION

From the events with Harvard CMT solutions, 68 events which lie on plate boundaries were selected for the inversion (*cf.* 20 events used by Pelayo & Wiens). All events were shallow (depth $\leq$ 60 km), since deeper events probably reflect intraplate deformation. Only thrust-type events with $m_b \geq 5.5$ were selected from the South Sandwich Trench to constrain SAN–SAM motion (Fig. 3). This, together with the depth criterion, also avoids those earthquakes that may be associated with shallow–intermediate tearing of the subducted slab beneath the northern portion of the South Sandwich forearc. Events along the Shackleton Fracture Zone between 55°W and 66°W were excluded for the reasons discussed above. In addition, a second data set was prepared, including the moment tensor sums (Table 2) in place of the individual thrust events at the SAN–SAM boundary. Averages V and VI in the southern part of the trench were not used, owing to their low consistency.

Horizontal slip vectors were calculated from the Harvard CMT solutions (Jost & Herrmann 1989). Because every earthquake has two nodal planes with two corresponding slip vectors, we are confronted with an ambiguity in choosing one of them as the appropriate slip vector. For the selected events, it was clear from the plate geometry which nodal plane should be chosen. Those fault plane solutions that did not clearly correspond to the surface expressions of the local plate motions were generally found to correspond to deeper ($\geq$60 km) events or shallow events in a complicated tectonic regime, such as the unclear SCO–SAN–SAM triple junction region. The slip vectors of these events are listed in Table 1.

Focal mechanisms computed by Pelayo & Wiens (1989) using body waveform inversion methods were also included if they were awarded a solution quality of A or B by those authors. Where a Harvard CMT also existed for the same event, the mechanism of Pelayo & Wiens was preferred, owing to the more careful fitting of waveforms by the latter.

Using the iterative least-squares plate motion inversion technique of Minster *et al.* (1974), we inverted the chosen earthquakes, spreading rates and transform azimuths for a four-plate (ANT, SAM, SCO, SAN) model. Our implementation of the inversion procedure starts with an *a priori* model and iteratively fits for the best set of perturbations in angular velocity vectors using Cartesian coordinates. This procedure was chosen over that involving perturbations in latitude and longitude in order to avoid any possible instability near the geographic poles, where longitude perturbations tend to be large. The SAM–ANT Euler vector is held fixed and is prescribed by model NUVEL-1A (86.4°S, 139.3°E, 0.27 deg Myr^{-1}, DeMets *et al.* 1990, 1994).

We performed inversions for five different input files: (1) the original file, including all data from Table 1, (2) input file 2 without event 1 (PW2), since this South Georgia event may not lie on a plate boundary, as discussed above. Input file (3) is identical to input file 2 for all plate boundaries except SAN–SAM, for which the moment tensor sums (Table 2) with high consistency (I–IV) are used in place of individual thrust events. PW89 is the original Pelayo & Wiens (1989) input file and PW-1 is input file PW89 without event 1.

4 RESULTS

4.1 Euler poles and angular rotation rates

We obtained separate kinematic models by inversion of each corresponding input file from section 3. The resulting Euler poles and angular velocities are given in Table 3 together with their 1σ

Table 3. Euler rotation models with errors and chi^2 as derived from the inversion of the four input files (see text). The PW89 results are not given here. ⋆, geocentric degrees; ⋆⋆, azimuth of semi-major axis in degrees clockwise from due north. First named plate moves counter-clockwise relative to the second plate.

Plates	Lat. (deg)	Lon. (deg)	Rate deg Myr^{-1}	Error Ellipse Semi-maj.⋆	Error Ellipse Semi-min.⋆	Error Ellipse *Azimuth*⋆⋆	Error in ang. vel.	Red. chi^2	Input
SCO–SAM	−2.257	−56.538	0.071	32.531	2.828	176.950	0.021	0.13	Model 1:
SCO–ANT	−74.669	−69.561	0.282	2.367	0.932	209.490	0.043	(rates)	all events
SAN–ANT	−36.940	−32.619	1.409	6.472	1.000	171.199	0.417	1.20	from Table 1
SAN–SCO	−28.289	−30.210	1.212	10.309	1.219	176.416	0.388	(azi.)	
SAN–SAM	−27.037	−31.796	1.270	10.296	1.120	174.825	0.383		
SCO–SAM	23.760	−57.697	0.066	37.048	2.751	176.523	0.010	0.13	Model 2:
SCO–ANT	−74.994	−72.626	0.251	2.685	0.983	204.546	0.042	(rate)	as model 1
SAN–ANT	−36.383	−32.649	1.395	6.413	1.003	170.961	0.418	1.23	but without
SAN–SCO	−28.599	−30.417	1.222	10.152	1.202	176.136	0.390	(azi.)	No. 1 (P&W No. 2)
SAN–SAM	−26.318	−31.824	1.258	10.615	1.123	174.887	0.381		
SCO–SAM	19.074	−56.906	0.067	40.296	2.921	177.321	0.010	0.12	TLP2003:
SCO–ANT	−74.694	−71.267	0.257	2.574	0.987	206.451	0.047	(rate)	as model 2
SAN–ANT	−38.855	−34.551	1.571	5.218	1.554	169.304	0.430	1.44	but with
SAN–SCO	−32.248	−32.568	1.383	8.018	1.775	175.146	0.408	(azi.)	moment
SAN–SAM	−30.252	−33.787	1.421	8.459	1.733	174.135	0.402		tensor sum
SCO–SAM	88.924	48.277	0.351	7.741	0.350	80.287	0.201		model PW-1:
SCO–ANT	77.436	117.948	0.083	3.115	1.861	169.982	0.207		only P&W
SAN–ANT	−43.899	−28.698	2.796	5.875	0.644	180.049	1.213		events without
SAN–SCO	−44.859	−28.978	2.863	5.739	0.648	178.822	1.283		No. 1 (P&W No. 2)
SAN–SAM	−39.412	−28.797	2.629	8.018	0.684	180.313	1.191		

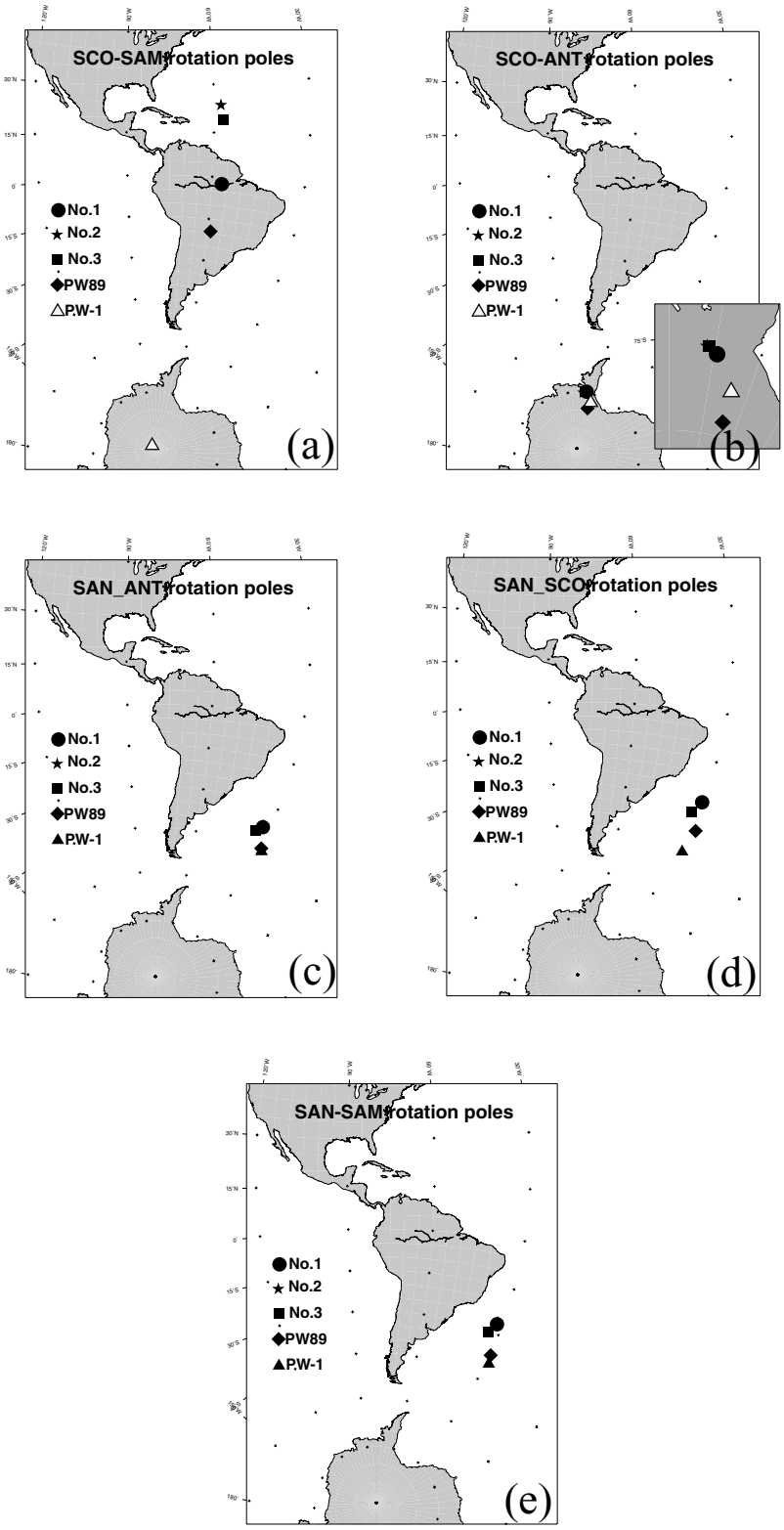

Figure 8. Euler poles derived from the inversion for five models as explained in the text. The first named plate moves counter-clockwise relative to the second plate. All maps are produced with the same projection area. (a) SCO–SAM rotation poles. For model PW-1, the SAM–SCO pole is shown (indicated by the white triangle). (b) SCO–ANT rotation poles, also shown in the inset. For model PW-1 the ANT–SCO pole is shown by the white triangle. (c) SAN–ANT rotation poles. (d) SAN–SCO rotation poles. (e) SAN–SAM rotation poles.

error ellipses and errors in angular velocities. Fig. 8 shows the Euler poles for all five models for each plate pair. Note that the antipodes of the SCO–SAM and SCO–ANT poles for model PW-1 are displayed (that is, the SAM–SCO and ANT–SCO rotation poles).

In general the poles for all models are similar, with the exception of the SCO–SAM poles (Fig. 8a), where models 2 and 3 lie more than 40° from PW89, and more than 70° from PW-1. The instability of model PW89 is demonstrated by the large differences between models PW89 and PW-1. In contrast, inversions of our more recent data sets (models 2 and 3) are stable with respect to the inclusion/exclusion of event 1 (models 1 and 3). Table 3 also shows the reduced χ^2 values for the rate data and the slip vector data. The values for χ^2 lie between 1 and 2 for the slip vector data, which indicates that our predictions of the errors (σ) in the data are reasonable.

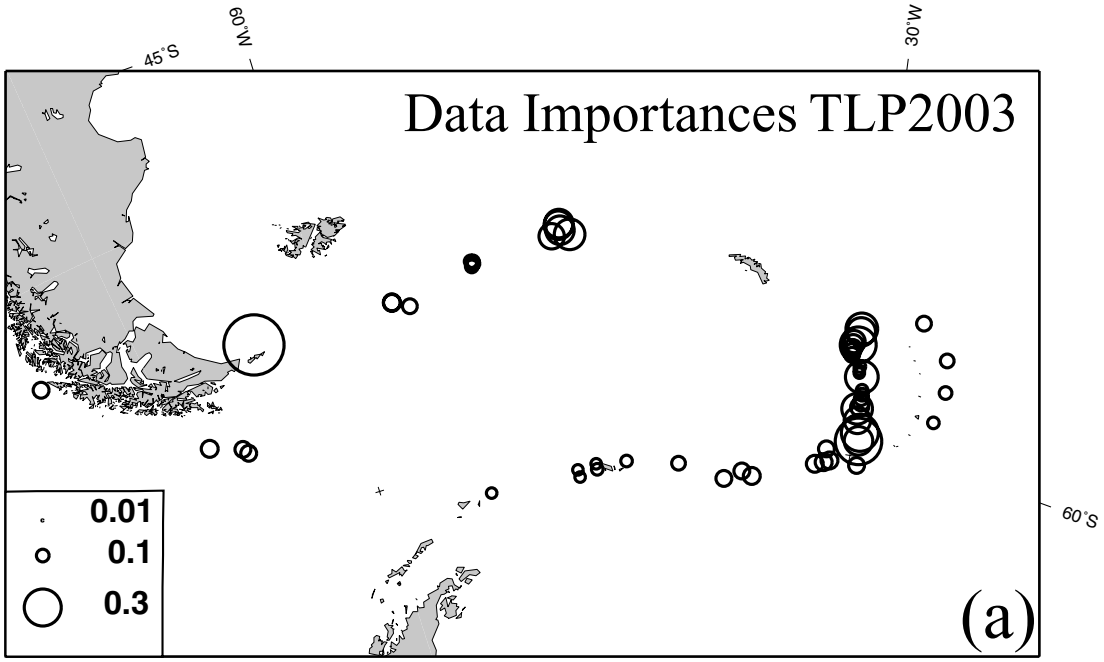

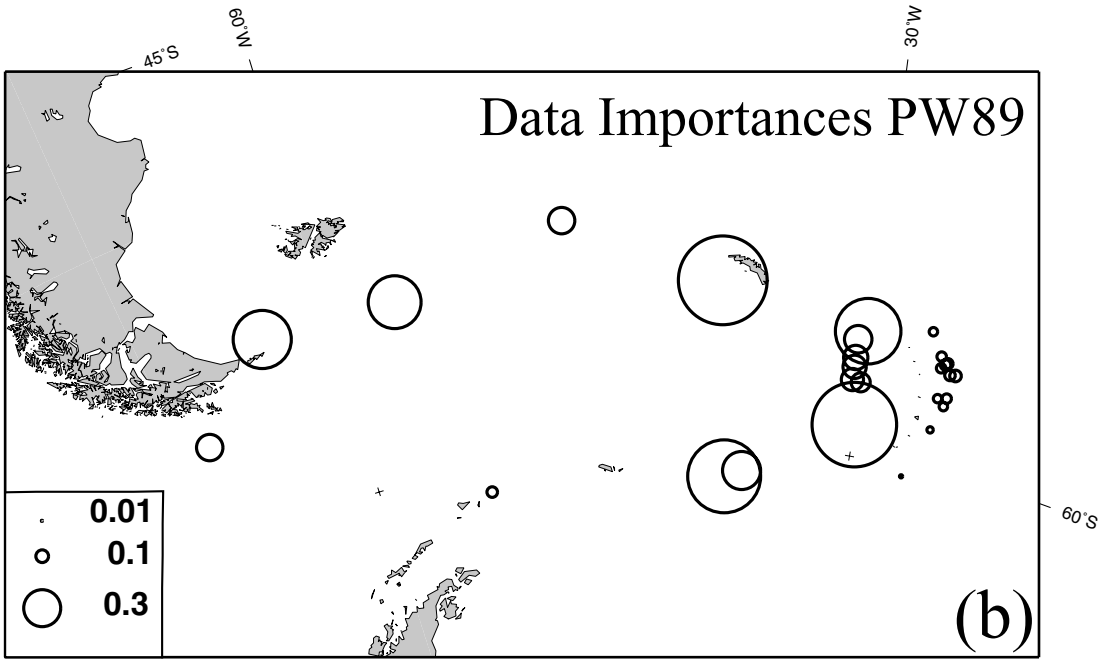

Figure 9. (a) Data importances for all data used for model 3 (TLP2003). The size of the circles is proportional to the value of the data importances, as indicated by the scale at the bottom left. (b) As (a) for model PW89 (original Pelayo & Wiens (1989) data file).

4.2 Data importances and uncertainties

Data importances give an indication of the contribution of each datum in the least-squares inversion (Minster *et al.* 1974), and sum to the number of degrees of freedom in the model. The data importances for model TLP2003 and model PW89 are shown in Fig. 9, where the diameters of the circles are proportional to the data importances. The lowest data importances in model 3 are for the moment tensor sums at the South Sandwich Trench, the SAM–SAN boundary (Fig. 9a). Importances at the South Scotia Ridge and at the Shackleton Fracture Zone are also small. The highest importances are at the northern and southern ends of the East Scotia Ridge (SAN–SCO) and on the North Scotia Ridge (SAM–SCO). The scatter in the distribution of the data importances is small compared with earlier results (model PW89, see also Fig. 9b), where we note that the South Georgia event has a disproportionately high importance (0.68).

Fig. 10 shows the 1σ error ellipses of models TLP2003 and PW89. The sizes of the SCO–SAM error ellipses in Fig. 10(a) are much larger than those in Fig. 10(b), but the errors in angular velocities are much smaller for TLP2003. The error ellipses are highly elongated in the north–south direction, which shows that the Euler vector is constrained on roughly a north–south line from the estimated pole. The larger uncertainties in Fig. 10(a) are due to the larger standard deviations on the input data compared with those in models PW89 and PW-1.

We believe that our study has benefited from the greater amount of data available since 1989, both CMT slip vectors and, especially, spreading rates and azimuths from the east Scotia Sea. This has resulted in a fairly uniform distribution of data importances (Fig. 9a). Fig. 11 shows the residuals between the observed datum and the predicted datum (also given in Table 1) for each event in our favoured data set, model 3, hereinafter referred to as model TLP2003.

5 DISCUSSION

Motions predicted by TLP2003 differ slightly from those of Pelayo & Wiens (1989), especially for the SAM–SCO boundary, for which the TLP2003 Euler pole lies 45° further north. Whereas Pelayo & Wiens' result predicted sinistral motions of ~5.0 ± 2.5 and 10.7 ± 2.4 mm yr^{-1} on the NSR and SSR, respectively, model TLP2003 predicts rates of ~7.1 ± 3.5 and ~7.7 ± 2.5 mm yr^{-1} on these two boundaries (Fig. 12, Table 4). At the South Sandwich Trench, the convergence rate varies from 69 ± 11 mm yr^{-1} in the north, to 78 ± 10.8 mm yr^{-1} in the south, with a WSW direction. The predicted backarc spreading vector is close to W–E, and varies from 62.5 ± 10 to 71.0 ± 10.2 mm yr^{-1}, north to south. In the case of the South Sandwich Trench and the East Scotia Ridge, the errors for the velocity vectors, calculated using the full model covariance matrix, are smaller for model TLP2003 compared with PW89; for the NSR and the SSR, however, the errors are slightly larger than for PW89 (Table 4).

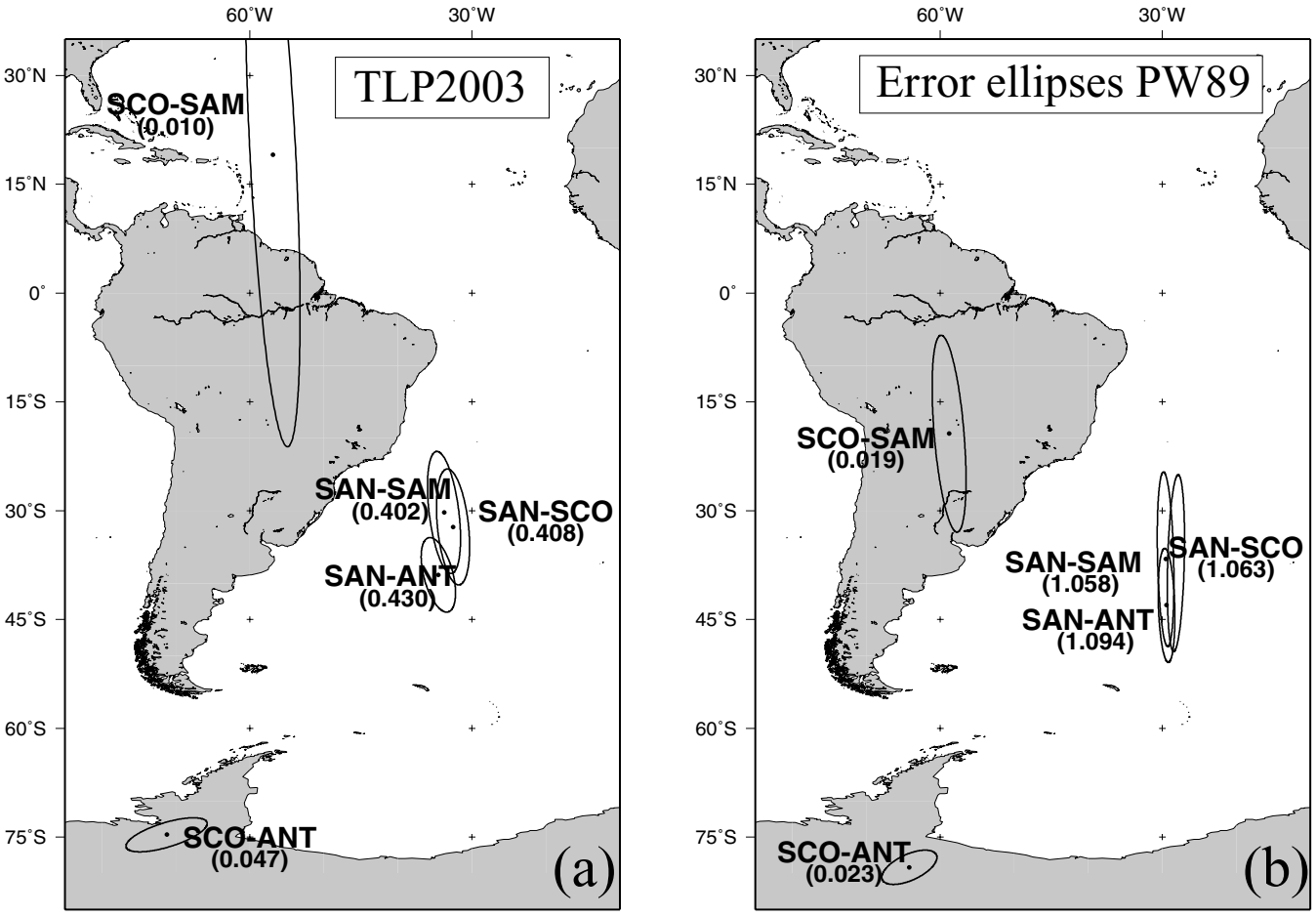

Figure 10. (a) 1–σ error ellipses for model 3 (TLP2003). The numbers in parentheses are the corresponding angular velocity in deg Myr^{-1}. (b) As (a) for model PW89.

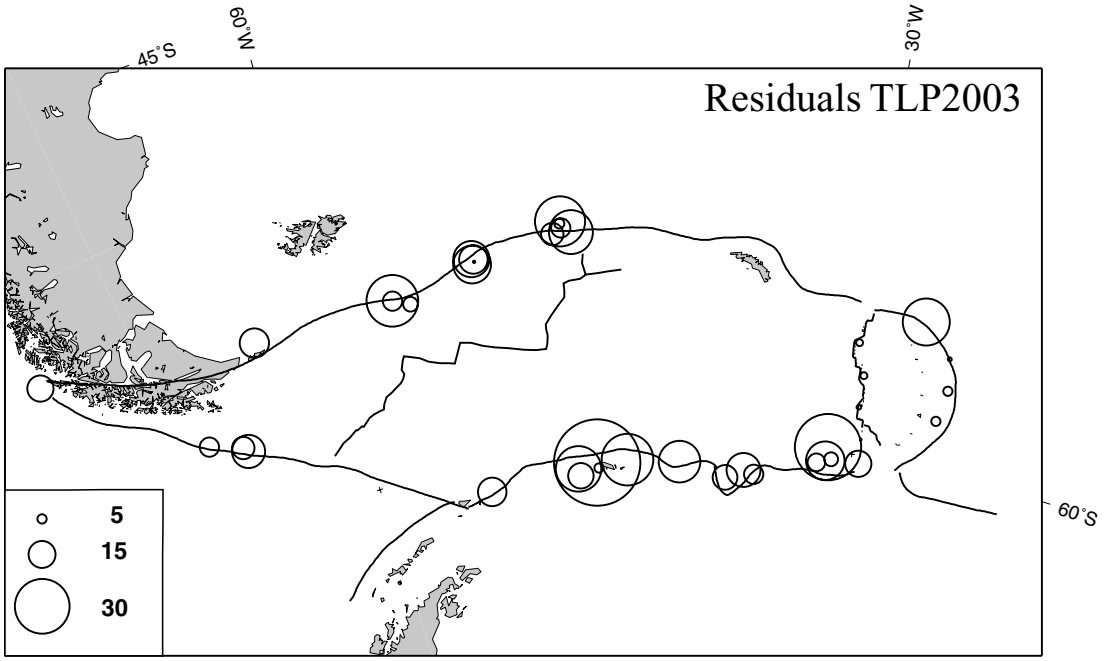

Figure 11. Residuals of the predicted datum and the observed datum for model 3, TLP2003 (see Table 1). The size of the circles is proportional to the residuals, as indicated by the scale at the bottom left.

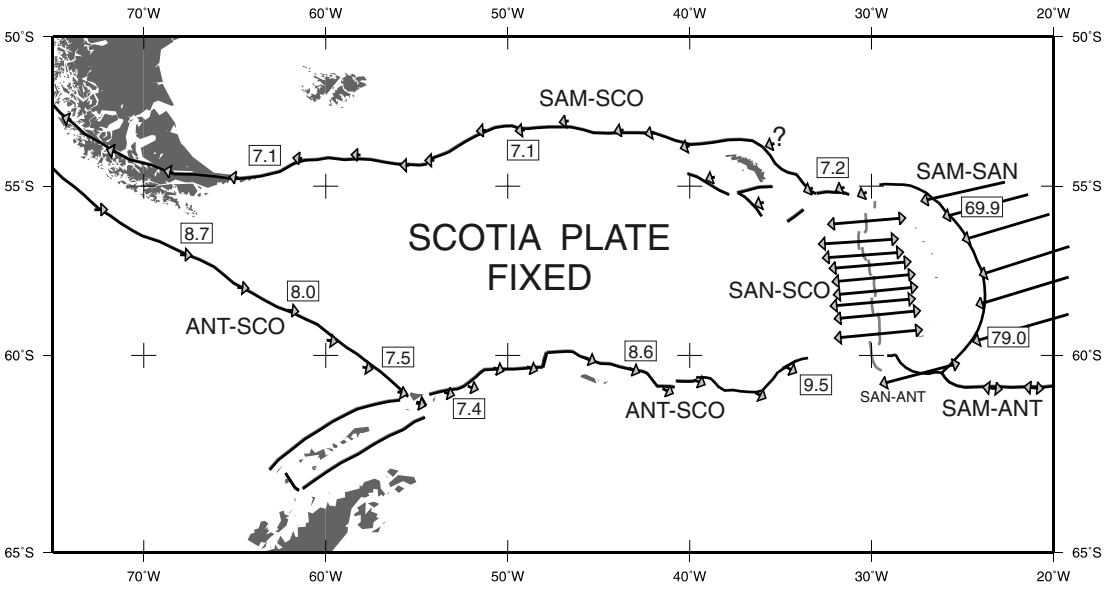

Figure 12. Velocity vectors along the plate boundaries as derived from model 3 (TLP2003).

Although the surface expression of the SCO–SAM plate boundary appears to lie north of South Georgia on the North Scotia Ridge, the only well-constrained seismic event (event 1 in Table 1, which is event PW2) indicates thrusting at the southern edge of the South Georgia block. Table 1 shows that the slip vector obtained by Pelayo & Wiens (1989) for event 1 agrees, within uncertainties, with the plate model TLP2003. Two further events occurred very recently at the southern margin of the South Georgia block (Fig. 3), also indicating SW-directed thrusting, and, like the earlier event, are associated with free-air lows. These results suggest that either the local deformation zone is very broad (approximately 200 km), perhaps involving independent motion of South Georgia, or the currently active plate boundary lies south of the South Georgia islands. Use of these events to constrain SCO–SAM motion would only be justified if South Georgia were now rigidly attached to South America. The absence of seismicity and the reduction in amplitude of free-air anomalies to the north and northeast of South Georgia, together with continuing thrusting to the south, suggest that this might indeed be the case.

To the northeast of South Georgia lies the Northeast Georgia Rise, a large Mesozoic igneous province. It is possible that the arrival of this feature, with its thickened, buoyant crust, at the formerly convergent SAM–SCO margin, impeded the eastward motion of South Georgia as part of the Scotia Plate (Vogt *et al.* 1976),

Table 4. Derived velocities along the main plate boundaries and uncertainties for model TLP2003 and PW89.

Plate boundary	Plates	Latitude (°S)	Longitude (°W)	PW89		TLP2003	
				velocity (mm yr^{-1})	error	velocity [mm yr^{-1}]	error
NSR	SCO–SAM	54	63	4.9	±2.5	7.0	±3.5
NSR	SCO–SAM	55	35	5.5	±2.6	7.1	±3.5
SSR	SCO–ANT	61	52	10.7	±2.4	7.7	±2.5
SST	SAN–SAM	55.3	26	67.7	±18.1	68.6	±11.0
SST	SAN–SAM	59	26	80.6	±19.4	77.8	±10.8
ESR	SAN–SCO	56	30	65.5	±15.7	62.5	±10.0
ESR	SAN–SCO	59.5	30	77.1	±18.6	71.0	±10.2

causing the South Georgia block to become disrupted into a series of fault blocks, between which strike-slip motion has occurred on NE-trending transcurrent faults. This would be analogous to the interaction of the Caribbean Plate with the Bahamas Platform near Hispaniola, causing rifting and microplate formation near Puerto Rico (Vogt *et al.* 1976; Masson & Scanlon 1991; Mann *et al.* 2002). Geodetic GPS measurements in the Caribbean (DeMets *et al.* 2000) indicate the existence of obliquely convergent motion, accompanied by strain partitioning, between the Caribbean (CAR) and North American (NAM) plates. This motion was not predicted by NUVEL-1A, or by several other studies based on earthquake slip vectors along the northern Caribbean Plate boundary (see Deng & Sykes 1995, for a discussion and references). On the other hand, studies by Frankel (1982), Sykes *et al.* (1982) and Deng & Sykes (1995) predicted an azimuth of N70°E for CAR–NAM motion, close to that observed using GPS satellites (DeMets *et al.* 2000).

Mann *et al.* (2002) used updated GPS measurements for the Caribbean and North American plates together with a more recent global reference frame to calculate a CAR–NAM Euler pole close to that of Deng & Sykes (1995). They favoured a strain-partitioning model with oblique slip occurring north of Hispaniola, and W–E strike-slip occurring on the Septentrional and Enriquillo faults. The striking similarity of the northern Caribbean and Scotia plate boundaries suggests the possibility that a similar obliquely convergent component may be present at the SCO–SAM boundary, yet undetected by our study.

Satellite and space geodetic studies in the Scotia Arc are at a very early stage, and results are not yet published for the SCO–SAM boundary. Moreover, apart from Tierra del Fuego, there are no land areas within the Scotia Plate from which to measure plate motion. Agreement between our predictions and preliminary observations on the Magellanes–Fagnano fault system (Schwartz *et al.* 2001; Smalley, personal communication) suggests that strain partitioning may be less significant at the North Scotia Ridge, and therefore an obliquely convergent component is unlikely. The presence of a linear free-air anomaly low along the North Scotia Ridge, together with evidence for a thrust plane beneath Burdwood Bank (see Section 3.1 above), indicates, nevertheless, that convergence has been important in the past.

Unlike the Caribbean Plate, which is subject to compression between the North American and South American plates, the Scotia Plate is bounded by major plates (South America and Antarctica) which, according to NUVEL-1A, are moving in a direction close to W–E in the Scotia Sea region. The Scotia Plate experiences only minor boundary forces from the East Scotia Ridge in the east, and the southern Chile Trench in the west, both in a W–E direction. The remaining driving forces must result from interactions at the northern, southern and western boundaries with the South American and Antarctic plates. Hence, there appears to be no net driving force in a N–S direction that could produce convergence at either the NSR or SSR.

On the other hand, pure strike-slip events on both the NW-trending Shackleton Fracture Zone and the WSW-trending western South Scotia Ridge cannot all represent SCO–ANT motion, so that partitioning must occur on one or both of these boundaries if the Scotia Plate is rigid. Pure strike-slip events on the southeastern Shackleton Fracture Zone were excluded from our inversion, as in PW89, on the grounds that this feature, like large-offset fracture zones elsewhere, tends to partition transpressional strain into an easily accommodated component parallel to the fracture zone, and more complex, possibly diffuse, deformation elsewhere. Pelayo & Wiens (1989) concluded that continued seismicity at the Phoenix Ridge reflects a diffuse zone of compression resulting from ANT–SCO convergence at the Shackleton Fracture Zone. Almost all epicentres SW of the Shackleton Fracture Zone lie on the extinct Phoenix Ridge axis, indicating post-spreading stress release. Focal mechanisms are predominantly strike-slip, but rotated with respect to the former spreading direction (Fig. 3), perhaps reflecting transmission of a compressional stress component from the Shackleton Fracture Zone to the fossil ridge axis.

6 CONCLUSION

Using a combination of earthquake slip vectors, spreading rates and azimuths, a robust solution for the plate motion of the Scotia Sea plates has been derived. The TLP2003 model is consistent with the NUVEL-1A model, and the inversion is stable with respect to the inclusion/exclusion of several marginally valid data, in particular an event that occurred to the SW of South Georgia. The 1σ error ellipses of Euler poles for all plate pairs involving the SAN plate overlap. Motions are consistent with the existence of a single, rigid, Scotia Plate, but SAM–ANT motion is distributed more evenly between the North Scotia Ridge and the South Scotia Ridge than previously thought.

The enhanced stability of our model compared with a previous model derived by Pelayo & Wiens (1989) is mainly due to the larger number of useful earthquakes and newly determined spreading rates and azimuths in the region.

ACKNOWLEDGMENTS

We would like to thank Chuck DeMets and Doug Wiens for their helpful and constructive reviews. Thanks also go to Heidi Stenner for pointing out some GPS results. All maps were produced using GMT (Wessel & Smith 1991).

REFERENCES

Aki, K. & Richards, P.G., 1980. Quantitative Seismology. Freeman and Company, New York, USA.

Applegate, B. & Shor, A., 1994. The northern mid-Atlantic and Reykjanes Ridges: spreading centre morphology between 55° 50′N and 63°00′N, *J. geophys. Res.,* **99,** 17 935–17 956.

Barker, P.F. & Burrell, J., 1977. The opening of Drake Passage, *Marine Geol.,* **25,** 15–34.

Barker, P.F. & Hill, I.A., 1981. Back-arc extension in the Scotia Sea, *Phil. Tran. R. Soc. Lond.* A, **300,** 249–262.

Bruguier, N.J. & Livermore, R.A., 2001. Enhanced magma supply at the southern East Scotia Ridge: evidence for mantle flow around the subducting slab?, *Earth planet. Sci. Lett.,* **191,** 129–144.

British Antarctic Survey, Teconic Map of the Scotia Arc, 1985.

Cunningham, A.P., Barker, P.F. & Tomlinson, J.S., 1998. Tectonics and sedimentary environment of the North Scotia Ridge region revealed by side-scan sonar, *J. geolo. Soc., Lond.,* **155,** 941–956.

DeMets, C., Gordon, R.G., Argus, D.F. & Stein, S., 1990. Current plate motions, *Geophys. J. Int.,* **101,** 425–478.

DeMets, C., Gordon, R.G., Argus, D.F., Stein, S., 1994. Effect of recent revisions to the geomagnetic reversal time scale on estimates of current plate motions, *Geophys. Res. Lett.,* **21,** 2191–2194.

DeMets, C., Jansma, P., Mattioli, G., Dixon, T., Farina, F., Bilham, R., Calais, E. & Mann, P., 2000. GPS geodetic constraints on Caribbean–North America plate motion, *Geophys. Res. Lett.,* **27,** 437–440.

Deng, J. & Sykes, L.R., 1995. Determination of Euler pole for contemporary relative motion of Caribbean and North American plates using slip vectors of interplate earthquakes, *Tectonics,* **14,** 39–54.

Dziewonski, A.M., Chou, T.-A. & Woodhouse, J.H., 1981. Determination of earthquake source parameters from waveform data for studies of global and regional seismicity, *J. geophys. Res.,* **86,** 2825–2852.

Eagles, G. & Livermore, R.A., 2002. Opening of Powell Basin, Antarctic Peninsula, *Mar. Geol.,* **185,** 195–205.

Ekström, G. & Engdahl, E.R., 1989. Earthquake source parameters and stress distribution in the Adak Island region of the Central Aleutian Islands, Alaska, *J. geophys. Res.,* **94,** 15 499–15 519.

Engdahl, E.R. & Gubbins, D., 1987. Simultaneous travel time inversion for earthquake location and subduction zone structure in the central Aleutian Islands, *J. geophys. Res.,* **92,** 13 855–13 862.

Engdahl, E.R., van der Hilst, R. & Buland, R.P., 1998. Global teleseismic earthquake relocation with improved travel times and procedures for depth determination, *Bull. seism. Soc. Am.,* **88,** 772–743.

Forsyth, D.W., 1975. Fault plane solutions and tectonics of the South Atlantic and Scotioa Sea, *J. geophys. Res.,* **80,** 1429–1443.

Frankel, A., 1982. A composite focal mechanism for micro-earthquakes along the northeastern border of the Caribbean Plate, *Geophys. Res. Lett.,* **9,** 511–514.

Frohlich, C. & Apperson, K.D., 1992. Earthquake focal mechanisms, moment tensors, and the consistency of seismic activity near plate boundaries, *Tectonics,* **11,** 279–296

Isacks, B., Oliver, J. & Sykes, L.R., 1968. Seismology and new global tectonics, *J. geophys. Res.,* **73,** 5855–5899.

Jarrard, R.D., 1986. Terrane motion by strike-slip faulting of forearc slivers, *Geology,* **14,** 780–783.

Jost, M.L. & Herrmann, R.B., 1989. A student's guide to and review of moment tensors, *Seismol. Res. Lett.,* **60,** 37–57.

King, E.C., Leitchenkov, G., Galindo-Zaldmvar, J., Maldonado, A. & Lodolo, E., 1997. Crustal structure and sedimentation in Powell Basin, in, *Geology and Seismic Stratigraphy of the Antarctic Margin Part 2, Antarctic Research Series,* Vol. 71, pp. 75–93, eds, Barker, P.F. & Cooper, A.K., AGU, Washington, DC.

Klepeis, K.A., 1994. The Magallanes and Deseado fault zones; major segments of South American–Scotia transform plate boundary in southernmost South America, Tierra del Fuego, *J. geophys. Res.,* **99,** 22 001–22 014.

Klepeis, K.A. & Lawver, L.A., 1996. Tectonics of the Antarctic–Scotia plate boundary near Elephant and Clarence Islands, West Antarctica. *J. geophys. Res.,* **101,** 20 211–20 231.

Larter, R.D. & Barker, P.F., 1991. Effects of ridge crest–trench interaction on Antarctic–Phoenix spreading; forces on a young subducting plate, *J. geophys. Res.,* **96,** 19 583–19 607.

Livermore, R.A., McAdoo, D.C. & Marks, K.M., 1994. Scotia Sea tectonics from high-resolution satellite gravity, *Earth planet. Sci. Lett.,* **123,** 255–268.

Livermore, R.A., Cunningham, A.P., Larter, R.D. & Vanneste, L.E., 1997. Subduction influence on spreading at the East Scotia Ridge, *Earth planet. Sci. Lett.,* **150,** 261–275.

Livermore, R.A. *et al.*, 2000. Autopsy on a dead spreading centre: the Phoenix Ridge, *Geology,* **28,** 607–610.

Ludwig, W.J. & Rabinowitz, P.D., 1982. The collision complex of the North Scotia Ridge, *J. geophys. Res.,* **5,** 3731–3740.

McCaffrey, R., 1992. Oblique plate convergence, slip vectors, and forearc deformation, *J. geophys. Res.,* **97,** 8905–8915.

Mann, P., Calais, E., Ruegg, J.-C., DeMets, C., Jansma, P.E. & Mattioli, G.S., 2002. Oblique collision in the northeastern Caribbean from GPS Measurements and geological observations, *Tectonics,* **21,** 1057, doi:10.1029/2001TC001304.

Masson, D. & Scanlon, K., 1991. The neotectonic setting of Puerto Rico, *Geol. Soc. Am. Bull.,* **103,** 144–154.

Minster, J.B., Jordan, T.H., Molnar, P. & Haines, E., 1974. Numerical modelling of instantaneous plate tectonics, *Geophys. J. R. astr. Soc.,* **36,** 541–576.

Pelayo, A.M. & Wiens, D.A., 1989. Seismotectonics and relative plate motions in the Scotia Sea Region, *J. geophys. Res.*, **94**, B6,7293–7320.

Sandwell, D.T. & Smith, W.H.F., 1997. Marine gravity anomaly from Geosat and ERS-1 satellite altimetry, *J. geophys. Res.,* **102,** 10 039–10 054.

Schwartz, D.P., Stenner, H.D., Smalley, R., Ellis, M. & Velasco, M.S., 2001. Paleoseismology at the end of the world: Initial observations of the Fagano Fault, Tierra Fuego, Argentinia, *Seismol. Res. Lett.,* **72,** 265.

Sykes, L.R., McCann, W.R. & Kafka, A.L., 1982. Motion of the Caribbean plate during last 7 Million years and implications for earlier Cenozoic movements. *J. geophys. Res.,* **87,** 656–676.

Tauxe, L., Herbert, T., Shackleton, N.J., Kok, Y.S., 1996. Astronomical calibration of the Matuyama–Brunhes boundary: consequences for magnetic remanence acquisition in marine carbonates and the Asian loess sequences, **140,** 133–146.

Taylor, B., Crook, K. & Sinton, J., 1994. Extensional transform zones and oblique spreading centers, *J. geophys. Res.,* **99,** 19 707–19 718.

Vogt, P., Lowrie, A., Bracey, D. & Hey, R., 1976. Subduction of aseismic oceanic ridges: effects on shape, seismicity, and other characteristics of consuming plate boundaries, Geological Society of America, Special Paper, **172,** pp. 33–42.

Wessel, P. & Smith, W.H.F., 1991. Free software helps map and display data, *EOS, Trans. Am. geophys. Un.,* **72,** 441, 445–446.

Wetzel, L.R., Wiens, D.A. & Kleinrock, M.C., 1993. Evidence from earthquakes for bookshelf faulting at large non-transform ridge offsets, *Nature,* **362,** 235–237.